A major purpose of the Technical Information Center is to provide the broadest dissemination possible of information contained in DOE's Research and Development Reports to business, industry, the academic community, and federal, state and local governments.

Although a small portion of this report is not reproducible, it is being made available to expedite the availability of information on the research discussed herein.

LA-UR 90-1483

Los Alamos National Laboratory is operated by the University of California for the United States Department of Energy under contract W-7405-ENG-36

TITLE: **Free-Electron Laser Physical Process Code FELPPC**

LA-UR--90-1483

DE90 011957

AUTHOR(S): L. Thode
D. Chan
M. Schmitt
J. McKee
J. Ostic
C. J. Elliott
B. McVey

SUBMITTED TO:

DISCLAIMER

Los Alamos
Los Alamos National Laboratory
Los Alamos, New Mexico 87545

Integrated Numerical Experiments (INEX) and the Free-Electron Laser Physical Process Code (FELPPC)

by

L. E. Thode, K. C. D. Chan, M. J. Schmitt,
J. McKee, J. Ostic, C. J. Elliott, and B. D. McVey

Abstract

The strong coupling of subsystem elements, such as the accelerator, wiggler, and optics, greatly complicates the understanding and design of a free electron laser (FEL), even at the conceptual level. Given the requirements for high-performance FELs, the strong coupling between the laser subsystems must be included to obtain a realistic picture of the potential operational capability. To address the strong coupling character of the FEL the concept of an Integrated Numerical Experiment (INEX) was proposed. Unique features of the INEX approach are consistency and numerical equivalence of experimental diagnostics. The equivalent numerical diagnostics mitigates the major problem of misinterpretation that often occurs when theoretical and experimental data are compared. The INEX approach has been applied to a large number of accelerator and FEL experiments. Overall, the agreement between INEX and the experiments is very good.

Despite the success of INEX, the approach is difficult to apply to trade-off and initial design studies because of the significant manpower and computational requirements. On the other hand, INEX provides a base from which realistic accelerator, wiggler, and optics models can be developed. The Free Electron Laser Physical Process Code (FELPPC) includes models developed from INEX, provides coupling between the subsystem models, and incorporates application models relevant to a specific trade-off or design study. In other words, FELPPC solves the complete physical process model using realistic physics and technology constraints. Because FELPPC provides a detailed design, a good estimate for the FEL mass, cost, and size can be made from a piece-part count of the FEL. FELPPC requires significant accelerator and FEL expertise to operate. The code can calculate complex FEL configurations including multiple accelerator and wiggler combinations. At the present time, the FELPPC assessment and evaluation code is being used in conjunction with a neural net to evaluate new concepts, perform trade-off studies, and perform initial design studies for a large number of FEL applications.

I. INTRODUCTION

A free electron laser is a complex and strongly nonlinear device. As such, the traditional approach of defining an interface between the various components of the system is difficult at best. Moreover, FEL performance is affected by strong coupling between the accelerator, wiggler, and optics. In fact, historically, FEL performance has been greatly reduced because this coupling has not been properly taken into account during the design phase of an experiment. In part, the coupling is determined by the evolution of the six-dimensional electron beam phase-space distribution. As a specific example, consider some of the issues associated with an electron beam accelerator, such as injector emittance and energy spread, longitudinal and transverse wakefields, cavity asymmetry, misalignments, and jitter. All these issues affect the electron distribution in a slightly different manner, but the effects are not independent of one another. The sum total of the effects determines the final state of the electron distribution function. Similar arguments apply to electron beam transport, wiggler transport, wiggler and resonator interaction, and energy recovery. Given the stringent requirements associated with high-performance FELs, the strong coupling must be taken into account in the evaluation and design process.

The Integrated Numerical Experiment (INEX) was proposed[1] to address the strong coupling nature of an FEL. In terms of the physics, INEX is a one-to-one numerical equivalent of the physical experiment. Engineering and technology constraints are included in the model to ensure that a given design is realistic. In some cases, INEX is used to set requirements such as control and alignment tolerances. In addition to the self-consistent nature of the integrated model, INEX includes numerical diagnostics that are equivalent to the physical diagnostics. In this fashion, the question of theoretical and experimental data interpretation, which is often a major source of discrepancy between theory and experiment, is avoided. Since validation against experiments is fundamental to the reduction of risk in any program, the incorporation of numerical diagnostics has significantly enhanced our ability to accurately evaluate a number of physics and technology experiments.

The INEX is constructed by linking a number of sophisticated physics programs, or codes, together in such a way that the evolution of electron phase space and light is determined in a consistent manner. Since precise knowledge of the electron phase-space distribution is required, the physics codes used in INEX are all particle transport codes. Particle codes calculate the dynamics of a small volume of phase space that is represented as a point particle. This type of code provides the most realistic description of particle dynamics and is used extensively to study complex problems in many areas of physics[2]. The three primary codes used in INEX are ISIS,[3] PARMELAX,[4] and FELEX.[5] In addition, there are a large number of secondary codes used to support the three primary codes, including MAFIA,[6] URMEL,[7] TBCI[8] and SUPERFISH.[9]

As a specific example of the INEX approach, consider the master-oscillator power-amplifier (MOPA) FEL configuration depicted in Fig. 1. The MOPA uses two different accelerators with separate FEL wigglers. A complete INEX calculation would calculate the electron beam evolution from the injector to the electron beam dump. As shown, ISIS and PARMELAX are linked to calculate the injector, low-energy accelerator, magnetic buncher, high-energy accelerator, and transport to the wiggler. At this point, the electron phase space distribution is linked to FELEX to calculate the FEL electron-wiggler interaction. After the FELEX calculation is completed, the residual electron phase-space distribution is linked back to PARMELAX for the electron beam dump calculation. In this case, a separate calculation is performed for both accelerators, because there is no direct link between the electron distribution functions.

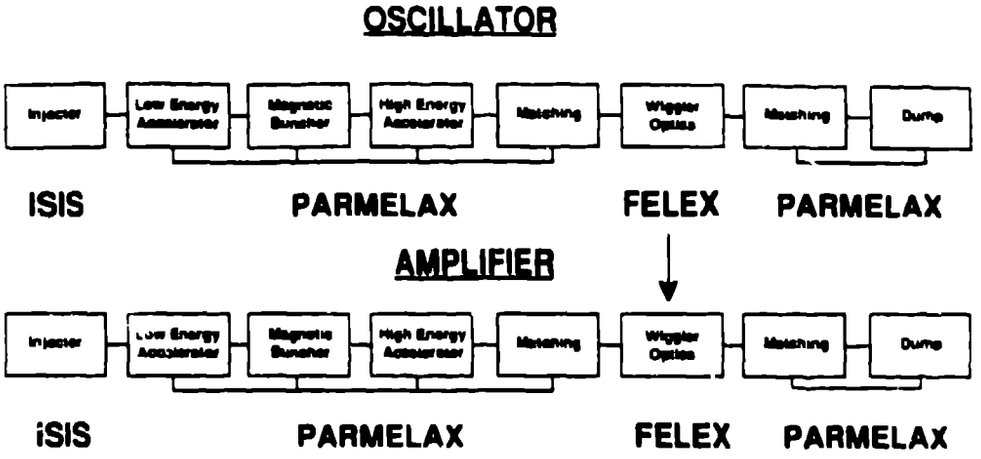

Fig. 1. Illustration of the linking of ISIS, PARMELAX, and FELEX for a master oscillator power-amplifier FEL system.

The link between the master oscillator and power amplifier is through the light pulse. FELEX provides this light link between the two wigglers. In this fashion, the FEL amplifier input signal includes the nonideal aspects of the light generated by the FEL oscillator. Although not presently a part of INEX, the evolution of light through the beam control system and output beam director could be calculated with GLAD[10] or OASIS2.[11]

When INEX was proposed, the linking between the various codes was to be performed with a controller IFEL.[12] At the present time, IFEL is only partly completed, with the link between PARMELAX and FELEX being manual. In addition, the link from FELEX back to PARMELAX is not complete.

Most of the INEX effort has been directed toward verification of the computational model with experiments. To date, the INEX model has been compared with eleven experiments, as summarized in Table I. In all cases, good agreement in terms of both scaling and magnitude has been obtained between INEX and the experiments. The success of the INEX approach has been the result of 1) a consistent treatment of the physics; 2) a number of improvements made in ISIS, PARMELAX, and FELEX; and 3) the use of numerical diagnostics equivalent to experimental diagnostics.

As an example, we consider the comparison of the High-Extraction-Efficiency experiment[13] with INEX. In this experiment four distinct wiggler configurations were investigated: 1) 12% linear taper in wavelength denoted by 12%, 2) 12% linearly taper in wavelength with a prebuncher denoted by 12% +, 3) 30% parabolic taper in wavelength 30% and 4) a 30% parabolic taper in wavelength with a prebuncher denoted by 30% +. Figure 2 is a comparison of the experimental results with the INEX predictions.

The purpose of the prebuncher, which is located upstream of the main wiggler entrance, is to induce a velocity modulation on the electron beam. In the drift space following the prebuncher, the velocity modulation is converted into a density modulation on the length scale of the optical wavelength. This prebunching allows a greater fraction of the electron beam to be captured in the decelerating bucket of the main wiggler. As a result, the extraction efficiency of the interaction can be increased, as can be seen by comparing the efficiency of the different wiggler configurations in Fig. 2.

Table I. Summary of accelerator and FEL experiments compared with the INEX.

Experiment		Location
#1	Proof-of-Principle Photoinjector Experiment	Los Alamos
#2	20-MeV Accelerator Experiment	Los Alamos
#3	Harmonic Experiment	Stanford
#4	10-μm FEL Mode Media Experiment	Los Alamos
#5	10-μm FEL Sideband Experiment	Los Alamos
#6	Cavity Asymmetry Experiment	Boeing
#7	10-μm FEL High-Extraction-Efficiency Experiment	Los Alamos
#9	Burst Mode 100-MeV Accelerator Experiment	Boeing
#10	0.6-μm Burst Mode FEL Experiment	Boeing
#11	HIBAF 17-MeV Accelerator Experiment	Los Alamos

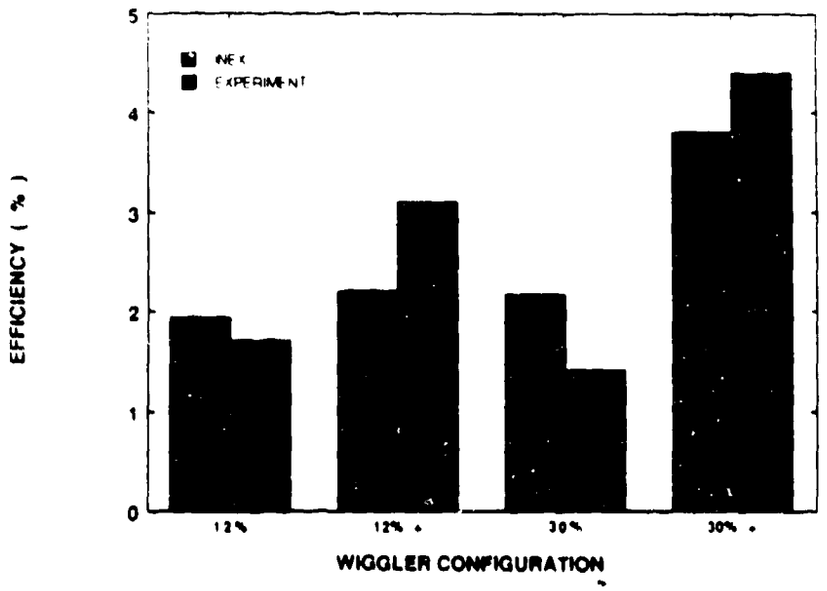

Fig. 2. Comparison between High-Extraction-Efficiency experiment and INEX predictions for four different tapered wiggler configurations.

Because the experiment used a conventional thermionic injector, the ISIS code was not used. PARMELAX was used to calculate the electron phase-space distribution up to the entrance of the wiggler and FELEX was used to calculate the FEL interaction. The overall agreement between INEX and the experiment is quite good.

Although the INEX approach has proved to be successful, the approach is difficult to apply to either a trade-off or initial design study. First, INEX requires a number of experts to operate because there are three primary codes and sixteen support codes required for a complete calculation. Second, because of the level of complexity of the calculations, the approach requires significant manpower to support a design effort. Finally, INEX requires a significant amount of computational time to complete the design process. In other words, the INEX approach is best suited for detailed final design.

FELPPC has been developed to overcome the disadvantages associated with the INEX approach. Basically, the idea was to use INEX as a guide for the development of realistic models for the accelerator, FEL interaction, and optics. Using these relatively simple models, an accurate prediction of FEL subsystem elements would be possible. In turn, the subsystem models could be coupled to obtain a system-like model for the FEL configuration. At the same time, the subsystem models would provide the detailed information required to estimate mass, cost, and size from a parts count. Finally, since much of the present interest in FELs is directed toward applications, the physics of the particular application of interest could be incorporated as a subsystem element into FELPPC. In this fashion, a relevant trade-off or initial design would always be performed in the context of the application.

At first, FELPPC might appear to be a system code, similar to other spread-sheet models developed for FEL applications. It is true that FELPPC takes an application oriented approach toward understanding a particular problem. However, FELPPC operates from a detailed physics description of specified hardware to obtain the performance from which the mass, cost, and size are determined. In general, there is no guarantee that FELPPC can provide the performance required for a particular application. As such, FELPPC is more akin to a design database for FEL configurations that includes nonideal effects. The application subsystem is simply used as a "metric" to judge the physics and technology implications of a particular FEL configuration.

FELPPC requires an expert to operate and is not a user-friendly "black box". What FELPPC offers is speed with credible physics. There can be hundreds of independent variables involved, depending upon the FEL configuration and application. As a result, some method is required to investigate the complicated nonlinear space described by FELPPC. We have chosen to use a neural net[14] for this purpose. To obtain optimal performance the neural net and FELPPC are combined with an optimization approach.

The entire process of neural net, FELPPC, INEX, and experiments is summarized in Fig. 3. Over the past few years the effort has concentrated on the development and verification of the overall approach, as indicated by the direction of the top arrow. At this juncture,

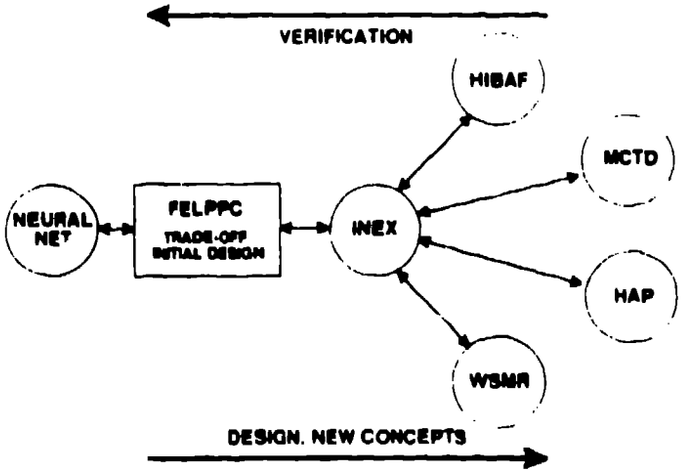

Fig. 3. The relationship between the neural net, FELPPC, INEX, and experiments is indicated. Here, HIBAF is the Los Alamos High Brightness Accelerator FEL, MCTD is the Boeing Modular Component Test Development experiment, HAP is the Boeing High Average Power experiment, and WSMR represents the GBFEL effort as an example of future experiments. The overall computational approach is applicable to any applied physics program.

we are beginning to reverse direction, as indicated by the bottom arrow; that is, we are simultaneously developing optimal designs for conventional FELs and investigating new concepts for accelerators, wigglers and optics. As new FEL regimes are investigated experimentally, we expect that some of the INEX and FELPPC models will prove to be inaccurate and the entire sequence of verification will need to be repeated. Overall, however, the ability to credibly extrapolate FEL technology will be significantly enhanced. In the longer term, it is hoped the computational methodology developed will benefit future applied physics programs.

In section II, an overview of FELPPC is presented. The eleven subsystem elements of the laser system are discussed: rf power, injector, accelerator beamline, magnetic buncher, magnetic bend, electron beam dump, oscillator, amplifier, energy recovery decelerator, beam control system, and output beam director. In addition, a short discussion of three application subsystems is given.

Some of the accelerator models are presented in Sec. III: the accelerator layout calculation, electron beam moments, and the cumulative beam breakup instability.

The FEL models are presented in Sec. IV: resonance conditions, wiggler magnetic fields, effective energy spread of nonideal electron beam distributions, small-signal gain, efficiency, and resonator optics.

Finally, a summary is presented in Sec. V.

II. FELPPC OVERVIEW

FELPPC is written in Fortran 77 and is designed to operate on the Los Alamos Cray system. Each problem investigated by FELPPC tends to be unique. Therefore, there are no defaults for the independent variables and constraints between independent variables must be constructed for each problem. As such, a user must be knowledgeable in accelerator and FEL physics as well as in the application under investigation. The code is maintained and modified using Historian.[15] Within limits, it is possible to plot any dependent variable as a function of any independent variable using Mapper[16] as a simple postprocessor. FELPPC can be operated interactively using namelist input. However, except for the initial evaluation of a problem, we expect FELPPC to be used primarily as a subroutine that is interrogated by a neural net.

FELPPC is still under active development. At the present time, Version II consists of about 17,000 lines of Fortran. Depending upon the complexity of the problem, FELPPC takes 1-5 seconds per design point when the cumulative beam breakup calculation is not requested. Typically, the timescale for calculation increases about an order-of-magnitude when the cumulative beam breakup instability calculation is utilized.

FELPPC first calculates the laser system performance, mass, cost, and size. There are eleven subsystem elements associated with the laser. In Table II, the function and subroutine name associated with each of these subsystem element is summarized.

A complex laser configuration can be constructed from these eleven subsystem elements. Each subsystem subroutine is indexed. The first index refers to the FEL configuration, whereas the second index refers to the subsystem element within that FEL configuration. For example, a master-oscillator power-amplifier laser system utilizes a separate FEL laser configuration for both the oscillator and amplifier. As such, both the master oscillator and power amplifier must be specified as distinct FEL configurations in FELPPC. At the same time, the master-oscillator and power-amplifier FEL laser configurations can be quite different. For the sake of argument, let the oscillator configuration be composed of an injector, an accelerator

Table II. FELPPC laser subsystem elements and corresponding subroutine names.

FEL Subsystem Element	Subroutine Name
rf Power	RFEFFIC (j)
Accelerator Injector	PHOTO (j,k)
Accelerator Beamline	BEAMLINE (j,k)
Magnetic Buncher	BUNCHER (j,k)
Magnetic Bend	ABEND (j,k)
Oscillator	OSC (j,k)
Amplifier	AMP (j,k)
Energy Recovery Decelerator	RECOVERY (j,k)
Electron Beam Dump	BEAMDUMP (j,k)
Optical Beam Control System	BCS (j)
Optical Output Beam Director	DIRECTOR (j)

beamline, an oscillator, and a beam dump while the amplifier configuration is composed of an injector, an accelerator beamline, a magnetic bend, an amplifier, another magnetic bend, an energy recovery decelerator, and a beam dump. The FELPPC construction of this laser system is shown in Table III. The rf power source, beam control system, and

Table III. Construction of a simple master-oscillator power-amplifier laser system. The oscillator contains six subsystem elements while the amplifier contains ten subsystem elements.

Laser Subsystem Element (Subroutine)	FEL Configuration (j)	Segment Number (k)
Oscillator rf power (RFEFFIC)	1	
Oscillator Accelerator Injector (PHOTO)	1	1
Oscillator Accelerator Beamline (BEAMLINE)	1	2
FEL oscillator (OSC)	1	3
Electron Beam Dump (BEAMDUMP)	1	4
Optical Beam Control System (BCS)	1	
Amplifier rf power (RFEFFIC)	2	
Amplifier Accelerator Injector (PHOTO)	2	1
Amplifier Accelerator Beamline (BEAMLINE)	2	2
Amplifier Magnetic Bend (ABEND)	2	3
FEL Amplifier (AMP)	2	4
Amplifier Magnetic Bend (ABEND)	2	5
Energy Recovery Decelerator (RECOVERY)	2	6
Electron Beam Dump (BEAMDUMP)	2	7
Optical Beam Control System (BCS)	2	
Optical Output Beam Director (DIRECTOR)	2	

output beam director subroutines are not indexed by element because each is only utilized once in a configuration. As constructed, the rf power source is allowed to be different for the oscillator and amplifier configuration. The beam control system for the oscillator configuration consists of the transfer optics between the oscillator and the amplifier and no output beam director is required. The actual beam control system and output beam director are associated with the higher output power amplifier configuration.

A. Rf Source Subsystem Element

For each FEL configuration, the efficiency associated with the specified rf source is determined using the RFEFFIC subroutine. At present, there are six sources that can be selected: 1) solid state, 2) tetrode, 3) klystron, 4) crossfield amplifier, 5) lasertron, and 6) klystrode. The efficiency of each source is a function of the rf frequency. In addition, each source has a specific frequency range of operation. If the frequency falls outside this operational frequency range, the efficiency of the source becomes small. In this manner, during optimization, each source is effectively limited to the correct operational regime. For each source a risk value must be assigned: low, medium, or high. Generally, the higher the risk, the higher the efficiency of the source.

B. Accelerator Subsystem Elements

The accelerator performance, mass, cost, and size are calculated by the subroutines PHOTO, BEAMLINE, BUNCHER, and ABEND. The functional block diagram for these accelerator subsystem elements is depicted in Figs. 4 through 7. In many instances, the functional blocks correspond to additional subroutines.

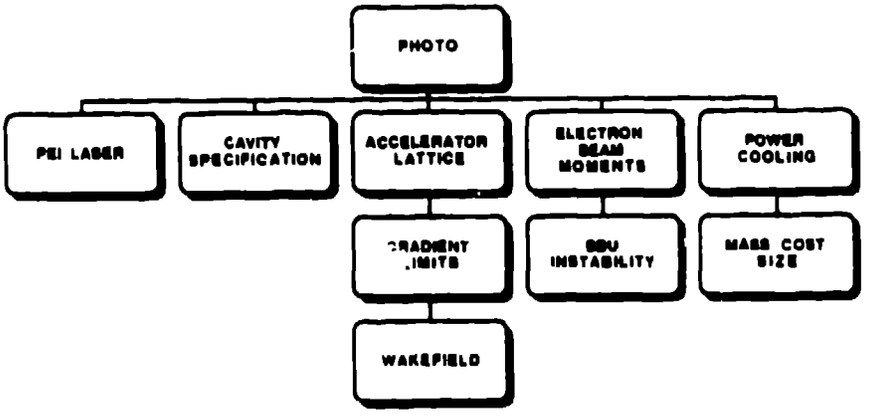

Fig. 4. Functional block diagram of the subroutine PHOTO for the injector subsystem element. The order of calculation is from left-to-right and top-to-bottom.

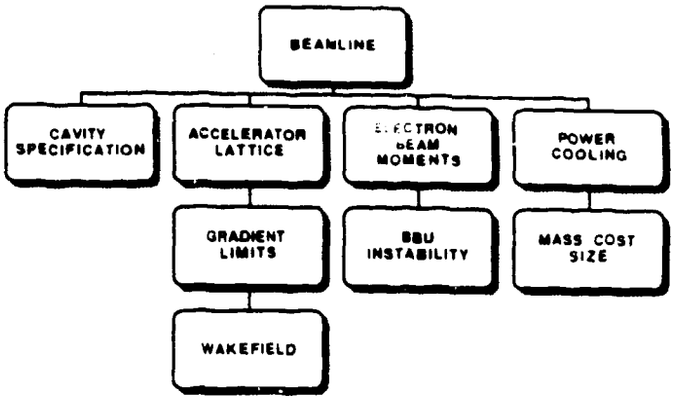

Fig. 5. Functional block diagram of the subroutine BEAMLINE for the accelerator beamline subsystem element. The order of calculation is from left-to-right and top-to-bottom.

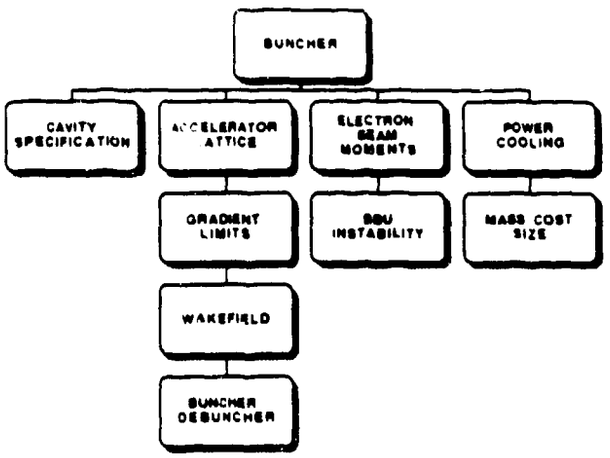

Fig. 6. Functional block diagram of the subroutine BUNCHER for the magnetic buncher subsystem element. The order of calculation is from left-to-right and top-to-bottom.

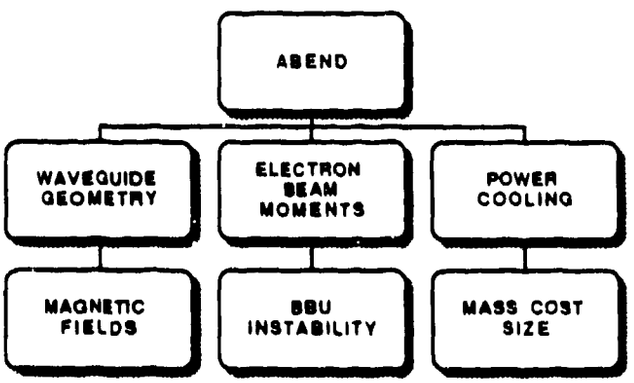

Fig. 7. Functional block diagram of the subroutine ABEND for the magnetic bend subsystem element. The order of calculation is from left-to-right and top-to-bottom.

In order to calculate the accelerator performance with some precision, the accelerator layout must be calculated correctly. First, the accelerator technology and associated hardware must be specified. It is possible to select pulsed or continuous-wave operation. The accelerator technology can be specified as cryogenic, conventional superconductor, or high-temperature superconductor. Room temperature operation is included as a subset of cryogenic technology. In addition, the accelerator cavity shape is a hardware option. At present, there are five cavity shapes in FELPPC, each with a data base generated by URMEL and TBCI. It is possible to select a thermionic injector or photoinjector. In addition, the magnetic buncher and magnetic bend types must be specified.

After the hardware is specified, the accelerator layout is calculated taking into account the rf frequency, rf source characteristics, cavity coupling, micropulse charge, peak current, operating temperature, average current, focusing, magnetic bunchers, and magnetic bends. In addition, there are a number of design constraints determined from a low, medium, or high risk specification: 1) breakdown limited electric field gradient, 2) rf window power limit, and 3) rf power source safety margin. Finally, the electron beam current pulse shape, the method for determining the cavity phase, and method for determining energy gain per subsystem element enter into the accelerator layout calculation.

The electron beam kinetic energy, peak current, average current, emittance, and energy spread are updated as FELPPC moves from element to element within an FEL configuration. First, micropulse emittance growth due to nonuniform fields, wakefields, and space charge is calculated. Second, micropulse energy spread growth due to space charge, wakefields, and magnetic bunching is calculated. Third, the micropulse moments are modified to take into account jitter and misalignment. Finally, emittance growth resulting from the cumulative beam breakup instability is determined. The cumulative beam breakup instability calculation includes jitter and misalignment, stagger tuning, focusing, and higher-order-mode coupler design.

From the accelerator layout, the power and cooling requirements are determined and the mass, cost, and size of each subsystem element is calculated. The subsystem element costs are obtained using mass categories with different specific costs. Because of the parts count approach, it is expected that the mass, cost, and size algorithms should provide reasonable scaling and magnitude estimates.

C. Amplifier and Oscillator Subsystem Elements

The conversion of electron beam kinetic energy into light is calculated by the subroutines AMP and OSC. In each case, the performance, mass, cost, and size is determined for each subsystem element. The functional block diagrams for the FEL subroutines are shown in Figs. 8 and 9. In many instances, the functional blocks correspond to additional subroutines.

As with the accelerator subsystem elements, hardware options must be specified for the FEL subsystem elements. First, the type of laser system configuration must be selected: 1) oscillator (OSC), 2) spontaneous emission amplifier (SEAMP), 3) conventional laser driven amplifier (CLAMP), 4) master-oscillator power-amplifier (MOPA), or 5) single-accelerator master-oscillator power-amplifier (SAMOPA). The FELPPC code requires knowledge of the laser system configuration to update electron beam moments, determine transfer optics, and determine the input amplifier power correctly. Second, the type of wiggler, mirrors, and resonator configuration must be specified. At present, there are five

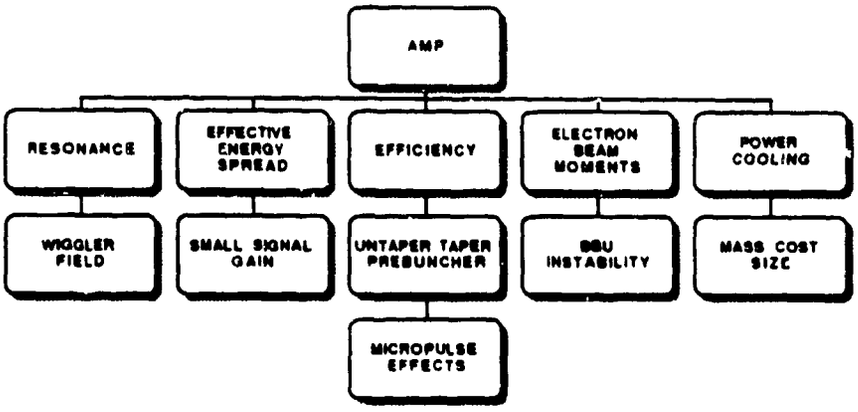

Fig. 8. Functional block diagram of the subroutine AMP for the FEL amplifier subsystem element. The order of calculation is from left-to-right and top-to-bottom.

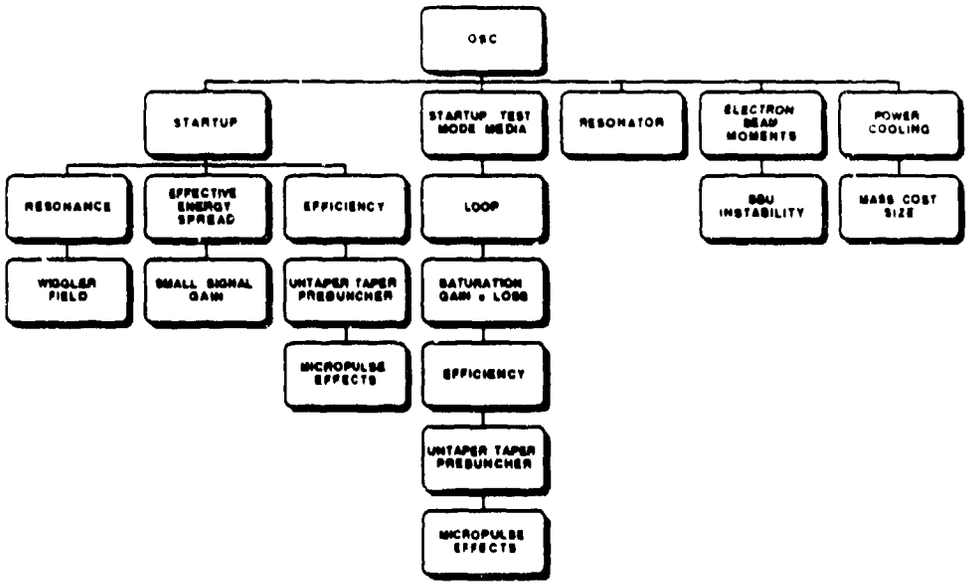

Fig. 9. Functional block diagram of the subroutine OSC for the FEL oscillator subsystem element. The order of calculation is from left-to-right and top-to-bottom.

wiggler options: permanent, hybrid, electromagnetic, superconducting, and pulsed. Metal or dielectric mirror can be specified. In some cases, the mirrors information is frequency dependent. The resonator options are 1) simple concentric, 2) ring, and 3) ring with a grating rhomb.

The AMP subsystem element first determines the resonance condition based upon the wiggler type and safety margins. At present, the safety margins are not options. Using the nonideal electron beam moments determined by the accelerator subsystem elements, the effective energy spread associated with the beam-wiggler combination is determined. The small-signal gain is then determined from the solution of an integral equation. At this point, it is possible to calculate the nonlinear conversion efficiency of electron beam kinetic energy into light, a calculation that includes the nonideal aspects of the electron distribution and micropulse effects. The ratio of the tapered-to-untapered wiggler length is determined from the nonlinear model. Moreover, if possible, a wiggler prebuncher is utilized to enhance efficiency.

The FEL interaction gives rise to energy spread growth on the electron beam, whose amplitude depends upon the efficiency of the interaction. In the AMP subroutine element the electron beam micropulse moments are updated for the energy recovery or electron beam dump calculations. At this point, the emittance growth from the cumulative beam breakup instability is calculated.

After determining the detailed amplifier performance, the power and cooling requirements are calculated. A parts count is then used to generate the mass, cost, and size of the amplifier subsystem element.

The oscillator subsystem element is more complicated than the amplifier subsystem element, as seen from Fig. 9. First, it must be determined if it is possible for the oscillator to startup. Because of mode mismatch resulting from gain, it is not sufficient that the small-signal gain simply exceed the resonator loss. Basically, depending upon the small-signal gain and resonator loss at saturation a safety margin is required to ensure startup.

If startup is possible, an iteration is performed to establish the oscillator operation point where saturated nonlinear gain equals the total resonator loss. As in the amplifier subsystem element, the nonlinear conversion efficiency is calculated with a nonideal electron distribution and micropulse effects. Again, the ratio of the tapered-to-untapered wiggler length is determined from the nonlinear model and, if possible, enhanced efficiency is obtained using a wiggler prebuncher. In addition, after startup, it is possible to enhance oscillator efficiency with a dynamic wiggler.

The resonator type is a hardware option. Resonator loss is calculated from the number and reflectivity of elements in a particular resonator. The outcoupling efficiency is an independent variable. Both the resonator loss and outcoupling efficiency enter into the saturation calculation. The mirror and resonator size are calculated taking into account distortion and electron-light overlap.

Even if the oscillator interaction is weak, as occurs for a SAMOPA configuration, electron beam energy spread is induced on the electron beam. In the OSC subsystem element the electron beam micropulse moments are updated for the following accelerator, amplifier, energy recovery, or electron beam dump calculations. Again, the emittance growth from the cumulative beam breakup instability is determined.

Given the detailed oscillator performance, the power and cooling requirements can be calculated. A parts count is then used to generate the mass, cost, and size of the oscillator subsystem element.

D. Energy Recovery Decelerator Subsystem Element

The energy recovery decelerator performance, mass, cost, and size are calculated in subroutine RECOVERY. The functional block diagram for the RECOVERY subroutine is shown in Fig. 10. In some instances, the functional blocks correspond to additional subroutines.

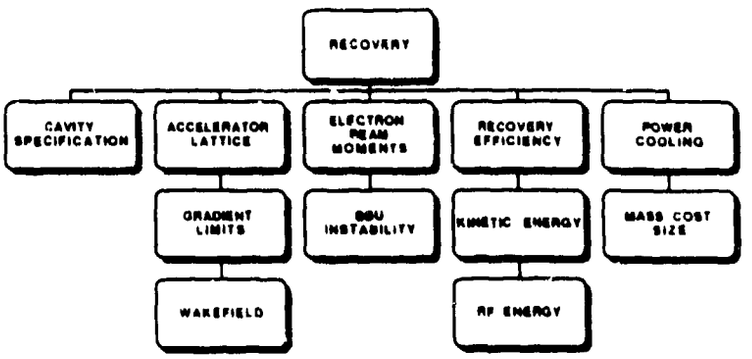

Fig. 10. Functional block diagram of the subroutine RECOVERY for the energy recovery decelerator subsystem element. The order of calculation is from left-to-right and top-to-bottom.

There are a number of hardware options for RECOVERY. The accelerator and decelerator must have identical operation and technology: pulsed or continuous-wave operation and cryogenic, conventional superconductor, or high-temperature superconductor technology. To start, a same-structure or parallel-structure configuration must be specified for the decelerator. Here, same-structure energy recovery implies that the accelerator and decelerator are the same structure. Parallel-structure energy recovery implies that the accelerator and decelerator structures are separate, but are coupled together in parallel. The cavity shape is a hardware option. Thus, in the parallel-structure configuration the accelerator and decelerator can have different cavities.

At present, the energy recovery is composed of two parts. First, the fraction of the residual electron beam kinetic energy recovered is calculated. The residual electron beam power from the kinetic energy recovery process must be handled by the electron beam dump. Second, the fraction of the recovered kinetic energy available for rf power in the acceleration process is calculated.

As the electron beam kinetic energy is converted into light, an energy spread is induced on the electron beam. The higher the FEL conversion efficiency, the larger the electron beam energy spread. A special energy recovery bend is used to disperse the electron beam along the direction of propagation in correlation with the electron energy[17]. The FEL interaction and deceleration are distinct nonlinear processes. Consequently, it becomes more difficult for the decelerator to "put the electron distribution back together" as the FEL conversion efficiency increases.

The kinetic energy recovery efficiency also depends upon the cumulative beam breakup instability. In the decelerator the electron kinetic energy decreases as the beam propagates along the structure. As a result, the beam becomes more sensitive to transverse deflecting forces as the decelerator continues to remove kinetic energy. (Incidentally, with same-structure energy recovery the situation is more difficult because the magnetic focusing force is mismatched.) At some point the electron beam kinetic energy becomes too low for

the beam to be controlled, and the deceleration must be truncated. The energy recovery efficiency is sensitive to this truncation energy.

Once kinetic energy is removed from the electron beam, the fraction of the energy lost in the walls of the rf cavities must be calculated. The rf heating depends upon the accelerator technology, cavity type, operation temperature and frequency, and deceleration electric field. In turn, the deceleration electric field depends upon the truncation energy determined by the cumulative beam breakup instability.

Once the decelerator layout, cooling, and recovery efficiency are determined, the mass, cost, and size of the decelerator can be calculated. The choice of same-structure or parallel-structure recovery significantly impacts these parameter.

E. Electron Beam Dump Subsystem Element

The subroutine BEAMDUMP is intended to calculate the residual electron beam transport and electron beam dump performance, mass, cost, and size. At present, the residual electron beam transport model is not fully developed. The electron beam dump mass, cost, and size are determined from the residual electron beam kinetic energy and average power, which depend upon the previously calculated FEL and energy recovery efficiencies.

F. Beam Control System and Output Beam Director Subsystem Elements

The subroutines BCS and DIRECTOR calculate the performance, mass, cost, and size of the beam control system and output beam director, respectively. Simple algorithms are presently used. The efficiency of each subsystem depends upon the number of mirrors, vignetting, and reflectivity. Metal or dielectric mirrors can be specified. In some cases, the mirror information is frequency dependent. At present, jitter, vibration, and alignment, which are important for some applications, have not been implemented.

G. Application Subsystems

Application subsystems are provided as a "metric" against which a particular FEL configuration can be evaluated. At present, there are three application subsystems: 1) continuous-wave space-based FEL ICBM booster mission, 2) continuous-wave ground-based FEL cost, and 3) pulsed compact FEL cost.

There are a large number of models that make up the space-based FEL application subsystem. Specifically, this subsystem application includes standby and startup power; prime power; cooling; reactants; power conditioning; platform structure and harding; attitude, tracking, and pointing; attitude control; propulsion; ICBM booster mission; and constellation sizing and launch.

Typically, cost is not thought to be an application. However, in the context of FELPPC cost is a valid "metric" for evaluation. The two cost application subsystems contain more extensive estimates than the standard mass, cost, and size information provided by the subsystem elements.

III. ACCELERATOR MODELS

In this section, some of the accelerator performance algorithms are discussed. A complete discussion of all the algorithms, including the mass, cost, and size, is beyond the scope of the present article. Our goal is simply to provide the reader with an idea of the level of complexity of models used in FELPPC.

A. Photoinjector Laser

Define f_b as the micropulse frequency and Q_{micro} as the micropulse charge. The rf frequency must be an integer multiple of the micropulse frequency. Therefore, the average accelerator current is

$$I_a = f_b Q_{micro} \quad . \tag{1}$$

For pulsed operation Eq. 1 represents the average current during the macropulse.

For a photocathode excited by green light the required photoinjector laser power is given by

$$P_g = 2.36 I_a / \eta_q \tag{2}$$

where η_q is the photocathode quantum efficiency. If η_{pei} is the photoinjector laser efficiency, the electrical power required to generate the electron beam is

$$P_{pei} = P_g / \eta_{pei} \quad . \tag{3}$$

These three relations are used to estimate the power, cooling, mass, cost, and size of the photoinjector laser.

B. Accelerator Lattice Calculation

There are two options for the accelerator lattice calculation. First, an accelerator element can have a specified kinetic energy gain such that the required rf power must be calculated. Second, the rf power can be specified and the resultant kinetic energy gain can be calculated. The choice of either option depends upon the problem under investigation. The mathematical model used is the same for both options; only the solution approach is different. Only the latter option will be discussed here

The lattice calculation assumes a coupled π-mode structure in order to determine the spacing between acceleration cavities. A tank is defined as a collection of coupled cavities and a limit is set on the rf power feed. There is no coupling between tanks. Therefore, an uncoupled structure is made up of tanks with only one acceleration cavity. The tank separation is determined from the intercavity coupling coefficient (which depends upon a number of variables and design issues).

Once the rf power feed limit is specified, the tank design can be calculated. Define η_{lw} as the rf lines and windows efficiency and η_{safe} as the safety and control margin efficiency. Both of these efficiencies are defined on the basis of risk. Let P_{tube} be the rated rf power

level of the rf source and P_{limit} be an upper bound estimate for the tank rf power feed. This limit can be set by rf window breakdown, the rf waveguide layout, or the rf source itself. Given these power levels, the number of tanks that can be driven by the specified rf source is

$$N_{tank} = \eta_{lw}\eta_{safe}P_{tube}/P_{limit} \quad . \tag{4}$$

This is only the initial estimate for the number of tanks. If a tank structure becomes too long or contains too many cavities, the number of tanks driven by the specified source will be increased. Given the number of cavities per tank, the rf power feed limit per tank is

$$P_{feed} = \eta_{lw}\eta_{safe}P_{tube}/N_{tank} \quad . \tag{5}$$

There are four limits associated with the design of an individual cavity: 1) rf power, 2) heat generation, 3) Kilpatrick, and 4) specified. The rf power limit is

$$P_{feed} = [I_a \delta E_p \cos\phi + (\delta E_p)^2/ZT^2] \quad , \tag{6}$$

where ϕ is the rf phase angle and ZT^2 is the cavity shunt impedance times the square of the transit time factor. Here, δE_p is the kinetic energy gain across the cavity at zero rf phase. In Eq. 6, both the kinetic energy gain and the rf phase are unknown and must be determined by an iterative approach.

The second limit is associated with rf wall power. In this case, δE_h is determined by keeping the rf wall power below the cooling capacity P_{heat}:

$$P_{heat} = (\delta E_h)^2/ZT^2 \quad . \tag{7}$$

The third limit is due to electric field breakdown. The Kilpatrick limit relates the rf frequency to the maximum electric field strength, E_K, on the cavity surface:

$$f = 1.643E_K^2 \exp(-8.5/E_K) \tag{8}$$

and

$$\delta E_K = (KE_K/G)(\lambda/2) \quad , \tag{9}$$

where K is the Kilpatrick factor, G is the cavity enhancement, and λ is the wavelength. The Kilpatrick factor is how far above the Kilpatrick limit one would operate and is determined from a specified risk level. The cavity enhancement factor is defined as the ratio of the average acceleration gradient across the cavity to the maximum electric field on cavity surface, and it is obtained from a cavity data lookup table.

In some cases, the user may wish to specify an upper bound for the kinetic energy gain, δE_s. This option allows one to tailor the design to investigate the trade-offs between acceleration and rf wall power.

As a initial guess, the design kinetic energy gain is then determined by

$$\delta E = \text{minimum}\{\delta E_p, \delta E_h, \delta E_K, \delta E_s\} \quad . \tag{10}$$

An iteration is then carried out to determine δE such that

$$P_{feed} = N_{tank}^{cav}[I_a \delta E \cos\phi + (\delta E)^2/ZT^2] \quad , \tag{11}$$

where N_{tank}^{cav} is the number of cavities in a tank. The reduction of δE due to wakefields is then calculated. The final value of δE satisfies

$$P_{feed} = N_{tank}^{cav}[I_a \delta E \cos\phi + (\delta E)^2/ZT^2 + P_{wake}] \quad ,$$

where P_{wake} is the power converted into higher order modes during the acceleration process.

The length of a tank is determined by

$$L_{tank} = N_{tank}^{cav}(\lambda/2) \quad . \tag{12}$$

As a next step the tank separation, S, is determined. The coupling between the tanks is given by

$$\frac{1}{10Q_{ext}} = C_1 \exp(-\frac{C_2 S}{a}) \quad , \tag{13}$$

where

$$Q_{ext} = \frac{Q}{1 + \frac{P_{cav}}{P_{wall}}} \quad . \tag{14}$$

Here, P_{cav} and P_{wall} are the total power required for the cavity and the rf power dissipated in the cavity wall, respectively. The coupling coefficients C_1 and C_2, the cavity aperture radius a, and the cavity intrinsic Q are determined from a cavity data lookup table.

The electron beam kinetic energy is now known as a function of tank position. A FODO array is used to provide electron beam focusing between the tanks. Design of such an array can be found in Ref. 18. The periodicity of the focusing system is chosen to be twice the sum of the tank and tank separation length. Given a phase advance and the focal length, the required quadrupole magnetic field strength can then be calculated for each tank. These focusing fields are utilized in the cumulative beam breakup instability calculation. The radius of the beam, r_b, is calculated as a matched beam to the FODO array.

Knowing the number of tanks, the number of cavities, the number of magnets, the rf power and the rf heat load, the mass, cost, and size of the accelerator can be estimated.

C. Electron Beam Emittance and Energy Spread

The models for the electron beam emittance and energy spread are based upon INEX calculations. The emittance is 90% normalized with units of π mm-mrad. The 90% kinetic energy spread has units of kilovolts.

1. Photoinjector

The correlated photoinjector emittance is

$$\epsilon = 10 + 3Q_{micro}(nC) \quad . \tag{15}$$

The kinetic energy spread is

$$\Delta E = 50 + N_{tank} N_{tank}^{cav} \delta W \quad , \tag{16}$$

where δW is the induced wakefield energy spread per cavity calculated from FINDDE.

2. Beamline

The beamline space charge emittance growth is

$$\delta \epsilon = 0 \quad . \tag{17}$$

The kinetic energy spread growth is

$$\Delta E = N_{tank} N_{tank}^{cav} \delta W \quad . \tag{18}$$

3. Buncher

The magnetic buncher space charge emittance growth is

$$\delta \epsilon = \frac{I_{bun}}{E_b} \left(\frac{\alpha_1}{r_b} + \alpha_2 + \alpha_3 r_b \right) \tag{19}$$

and

$$I_{bun} = I_{in} \frac{ln(I_{in}/I_{out})}{I_{in}/I_{out} - 1} \quad , \tag{20}$$

where I_{in} and I_{out} are the input and output peak micropulse current, E_b is the electron beam kinetic energy, r_b is the electron beam radius, and α_1, α_2, and α_3 are coefficients that depend upon the buncher configuration.

The kinetic energy spread growth is

$$\Delta E = \Delta E_b + N_{tank} N_{tank}^{cav} \delta W \tag{21}$$

where ΔE_b is the residual energy spread from the induced energy spread required for bunching.

4. Magnetic Bend

The magnetic bend space charge emittance growth is

$$\delta \epsilon = \frac{I_b}{E_b} \left(\frac{\sigma_1}{r_b} + \sigma_2 + \sigma_3 r_b \right) \quad , \tag{22}$$

where I_p is the peak micropulse current and σ_1, σ_2, and σ_3 are coefficients that depend upon the magnetic bend configuration.

The energy spread growth is

$$\Delta E = 0 \quad . \tag{23}$$

5. Jitter and Cumulative Beam Breakup Instability

Eqs. 15 through 23 do not include emittance growth due the cumulative beam breakup instability or energy spread due to charge jitter. These latter contributions are treated as uncorrelated emittance and energy spread growth when combined with the micropulse emittance and energy spread obtained from the above expressions. Typically, micropulse emittance growth is uncorrelated while the wakefield contributions to the energy spread are correlated.

D. Accelerator and Decelerator Cavity Specifications

Subroutine ACAVITY provides a cavity data lookup for accelerator calculations. The similar subroutine ECAVITY provides the cavity data lookup for the energy recovery decelerator calculation. The data computed includes cavity geometry, cavity field enhancement, cavity coupling coefficients, intrinsic Q value, and shunt impedance for the fundamental mode. In addition, the data includes the frequency, coupling impedance, and Q for the dipole mode. The data base corresponds to room-temperature cavities operating at a fundamental frequency of 433 MHz, see Table IV. The cavity data are scaled to the required operating frequency and temperature.

Table IV. Summary of the cavity data contained in ACAVITY and ECAVITY.

Cavity Parameters	ERX	MCTD	LA5	LA8	LA12
Aperture Radius (m)	3.81	2.50	5.00	8.00	12.00
Radius (cm)	23.07	23.50	30.00	30.00	50.00
Surface Area (m^2)	0.706	0.792	0.844	0.860	0.888
Shunt Impedance ($M\Omega$)	10.91	12.83	7.02	6.80	5.00
Q-value	33667	37812	46230	50344	53317
Field Enhancement Factor	5.0	5.0	2.0	2.0	2.0
Dipole Mode frequency (MHz)	847.4	811.9	643.4	641.1	612.7
Dipole Mode Shunt Impedance($M\Omega/m^2$)	24000	18021	5005	3280	1478
Dipole Mode Q-value	60207	63597	55196	56595	52367

An accelerator or decelerator cavity can have one of the five shapes: ERX, MCTD, LA5, LA8, and LA12. The ERX and MCTD shapes are typical of those designed with nose cones for high shunt impedance. In this case, ERX is the cavity shape used in Los Alamos FEL experiments, whereas the MCTD cavity shape is used for the MCTD experiment at the Boeing Aerospace Corporation. On the other hand, LA5, LA8 and LA12 are cavity shapes designed for beam stability. At 433 MHz they have an aperture radii of 5, 8, and 12 cm, respectively. The cavity shape resembles those used in a superconducting linac. The dipole mode coupling impedance is relatively low for all three of these cavities, possible to lower the dipole mode coupling impedance using a higher-order mode coupler. This collection of cavity shapes combined with the higher order mode coupler provides an adequate database for assessing the trade-off between accelerator efficiency and beam stability.

E. Wakefield Calculations

FINDDE allows FELPPC to compute the energy spread of a beam micropulse under the combined longitudinal force of the external rf accelerating voltage and the beam induced wakefield. In order to calculate the wakefield forces, the beam micropulse is divided into fifty-one longitudinal slices according to the specified electron current bunch shape. The presently available bunch shapes are Gaussian, parabolic, and square. The wake function of a slice, $G(\tau)$, is calculated according to

$$G(\tau) = C_1 \exp(-C_2\tau) + C_3 \exp(-C_4\tau) \cos(C_5\tau) \tag{24}$$

where τ is the distance behind the slice. The parameters C_n for the five cavities are contained in a database in subroutine ACAVITY. These coefficients were derived by least-squared fitting of wake functions calculated using the computer code TBCI.[8] Once the charge and wake function of a slice are known, the longitudinal wakefield forces on the bunch can be determined.

If the field gradient and the operating phase of the external rf accelerating field are specified, the subroutine will calculate the combined accelerating force on each slice due to the external rf and wakefield forces, from which the energy spread and average acceleration of the beam bunch can be calculated. In addition, the power lost by the beam to higher order modes of the cavity due to wakefields is computed.

There are two options associated with determining the operation phase of the external rf accelerating field. The operating phase can either be set by the user or the optimum operating phase can be calculated according to the method described in Ref. 19, where the energy spread of the micropulse is minimized. With this approach, the micropulse will be advanced in phase to compensate for the increase of the wakefield amplitude toward the end of the bunch. As a result, a minimum energy spread is induced across the micropulse.

F. Beam Breakup Instability Calculations

The beam breakup instability is caused by beam excitation of dipole modes in accelerator cavities. These modes can deflect the beam in the transverse direction causing effective emittance growth and beam loss. FELPPC includes two types of beam breakup phenomena: regenerative beam breakup and cumulative beam breakup. In the following paragraph, the treatment of these two instabilities are briefly described. For more information the reader should refer to references 20 and 21.

Regenerative beam breakup occurs in individual accelerating tanks. An accelerating tank is composed of cavities whose dipole modes are electromagnetically coupled to one another. Investigation of the regenerative beam breakup has shown that there exists a threshold current for the instability. If the average current exceeds the threshold current, the beam power lost to the mode exceeds the mode resistive power loss in the tank. As a result, the deflecting mode will grow to large amplitude.

Unlike regenerative beam breakup, cumulative beam breakup occurs among tanks that are not coupled. The coupling of the deflecting modes between tanks is provided by the electron beam. The source of excitations of the deflecting modes can be divided into two categories: time independent and time dependent. The time-independent sources are misalignment of transport elements and accelerator cavities. Because these sources are time independent, they usually only induce a transient deflection of the beam and are not

harmful. Time-dependent sources include jitter of the input beam position, angle, and the micropulse charge. In this case, the excitation of the dipole mode will amplify the jitter in beam position resulting in an effective emittance growth.

In FELPPC, the cumulative beam breakup instability is included by tracking micropulses through the accelerator, wigglers, and decelerator. The tracking is done using a set of subroutines which include BBU, CUMBBU, LOOP, TRANS, and RESULT. The calculation allows for the specification of misalignment and jitter. The stabilizing effects of focusing, stagger tuning, and external higher-order-mode coupler can be included in the calculation. In the end, the presence of the instability leads to a reduction of the FEL interaction efficiency because of effective emittance growth.

IV. FREE-ELECTRON LASER MODELS

Several parameters must be specified so that a FEL can be designed. The following routines use parameter outputs from the accelerator routines previously described. These parameters include the electron beam energy, γmc^2, energy spread, $\Delta\gamma$, the emittance, ϵ, the peak electron beam current, I_p, and the average beam current, I_{ave}. The inputs required from the user include the lasing wavelength of the FEL, λ_s, the number of wiggler periods, N_w, and the specification of the FEL configuration. If an amplifier configuration is desired, the user must specify the laser power, P_{in}, injected into the wiggler. The user must also specify the type of wiggler to be used. A set of routines are called in series to evaluate the various FEL parameters. These routines design the wiggler, determine the effective energy distribution of the electron beam (provided by the accelerator routines) inside the wiggler, determine the small-signal gain of the FEL, determine the gain and efficiency of the FEL at saturation, and design the FEL optics. Each of these routines will be discussed in the following subsections.

A. Wiggler Design

The resonance condition determines the ratio of the radiation wavelength, λ_s, to the wiggler period, λ_w, for a given electron beam energy (in units of its rest mass), γ, and wiggler magnetic field amplitude, B_w. In general this relation has the form

$$\frac{\lambda_s}{\lambda_w} = \frac{1 - \beta_z}{\beta_z} \tag{25}$$

where β_z is the normalized electron velocity along the wiggler axis. For electron beams with $\gamma \geq 10$ this equation can be approximated by

$$\frac{\lambda_s}{\lambda_w} = \frac{1}{2\gamma^2}(1 + a_w^2/2) \quad , \tag{26}$$

where

$$a_w = \frac{|e|B_w\lambda_w}{2\pi mc^2} \tag{27}$$

is the normalized magnetic vector potential. As seen from Eqs. 26 and 27 the magnetic field amplitude, B_w, is required to evaluate the wiggler wavelength. The value of B_w

depends on the type of wiggler specified. The following wiggler types have been considered for FEL applications: 1) all permanent magnet wiggler, 2) permanent magnet and high-permittivity pole-piece combination, 3) conventionally cooled cw electromagnet, 4) superconducting electromagnet, and 5) pulsed electromagnet. For each of the wiggler types listed an algorithm for the peak on-axis magnetic field is given which depends on the gap, g, and the wiggler wavelength, i.e.

$$B_w = B_w(g, \lambda_w, \text{type}) \quad . \tag{28}$$

These relations in turn require that one know the wiggler gap. An approximate expression for g is given by

$$g(\text{cm}) = 0.3 + 5w(cm) \quad , \tag{29}$$

where w is the spotsize of the optical beam at the entrance to the wiggler. The constant factor of 0.3 cm arises from the need for a vacuum envelope around the electron beam inside the wiggler. A larger value of 0.7 is used for superconducting applications to allow room for the refrigeront. The factor of $5w$ insures that the optical intensity at the beam tube radius will not significantly affect the on-axis optical mode. The spotsize at the wiggler entrance is typically twice the diffraction limited spotsize, or

$$w = 2w_0 = 2\sqrt{\frac{z_r\lambda_s}{\pi}} = 2\sqrt{\frac{L_w\lambda_s}{2\pi}} \tag{30}$$

where it has been assumed that the wiggler length, L_w, is twice the Rayleigh range, z_r, and the optical focus is at the center of the wiggler. For high-gain amplifiers, the radiation of the electron beam produces gain guiding that can significantly reduce the effects of optical beam diffraction in the wiggler. For this case one could conceivably focus the optical beam at the entrance to the wiggler and maintain a constant optical beam radius throughout the length of the wiggler, thereby reducing the wiggler gap. For such applications Eq. 29 can be modified, provided the gain guiding conditions can be met under all operating conditions. Using Eqs. 26-30 and knowing that $L_w = N_w\lambda_w$, where N_w has been specified, the wiggler wavelength and magnetic field are uniquely determined.

B. Electron Beam Effective Energy

The effective energy distribution of the electron beam is required to determine the small signal and saturation characteristics of the FEL. The effective energy distribution of an electron beam is the distribution of the electrons with respect to axial velocity, β_z, or axial energy, $\gamma_\parallel$, related by

$$\gamma_\parallel = (1 - \beta_z^2)^{-1/2} \quad . \tag{31}$$

An electron's axial energy is a function of its initial transverse position and velocity (due to the finite emittance of the electron beam) and the wiggler magnetic vector potential. We have

$$\gamma_\parallel = \frac{\gamma(1 + a_w^2(0)/2)^{1/2}}{\left(1 + a_w^2(r)/2 + \gamma^2\beta_x^2 + \gamma^2\beta_y^2\right)^{1/2}} \tag{32}$$

where

$$a_w(r) \simeq a_w(0)\left(1 + \frac{k_w^2 r^2}{2}\right) \tag{33}$$

gives the transverse dependence of the wiggler magnetic vector potential near the wiggler axis. To calculate the effective energy distribution, the emittance and energy spread distributions must be known. The emittance for an azimuthally symmetric electron beam is given by

$$\epsilon = \pi \bar{r} \bar{\beta}_r \tag{34}$$

where

$$\bar{r} = \sqrt{\frac{\bar{x}^2 + \bar{y}^2}{2}} \qquad \bar{\beta}_r = \sqrt{\frac{\bar{\beta}_x^2 + \bar{\beta}_y^2}{2}} \tag{35}$$

are the average radial position and average transverse velocity. Assuming gaussian distributions in r, β_r, and $\gamma - \gamma_0$ we can write

$$F(\gamma_{eff}) = 4\pi^2 A \int_0^\infty d\gamma \int_0^\infty dr \int_0^1 d\beta_r \exp\left\{-\frac{(\gamma-\gamma_0)^2}{\Delta\gamma^2}\right\} \exp\left\{-\left[\left(\frac{r}{\bar{r}}\right)^2 + \left(\frac{\beta_r}{\bar{\beta}_r}\right)^2\right]\right\} \times \delta(\gamma_{eff} - \gamma_{\|}) \tag{36}$$

where $\gamma_{\|}$ inside the δ-function is given in Eq. 32 and A is a normalization constant. The integration of this expression can be performed provided the γ-dependence in the denominator of Eq. 32 can be eliminated. Since $(\gamma - \gamma_0)/\gamma \ll 1$ for the FEL beams being considered here, we can replace the exact energy, γ, in the denominator of Eq. 32 with the mean energy, γ_0, and perform the integrals, yielding[22]

$$F(\gamma_{eff}) = \frac{C^2 e^{-\chi^2}}{\pi\Delta\gamma}\left[1 - \sqrt{\pi}(\chi + C/2)\mathrm{erfc}(\chi + C/2)e^{(\chi+C/2)^2}\right] \tag{37}$$

where

$$\chi = \frac{\gamma_0 - \gamma_{eff}}{\Delta\gamma} \tag{38}$$

$$C = \frac{2\Delta\gamma\lambda_w a_w}{\epsilon\gamma_0^2}(1 + a_w^2/2) \tag{39}$$

and $\mathrm{erfc}(x)$ represents the conjugate error function[23] evaluated at x. The A coefficient has been determined by setting the integral of $F(\gamma_{eff})$ equal to unity. Plots of this function are given in Figs. 11 and 12. The effective energy distributions generated by a random sampling of gaussian emittance and energy spread distributions are also plotted for comparison. For small emittance ($\epsilon \Rightarrow 0$), the distribution is gaussian due to the intrinsic energy spread, $\Delta\gamma$. For relatively large emittance, the distribution exhibits the characteristic low-energy tail. From these distributions one can calculate the effective energy spread, $\Delta\gamma_{eff}$ by

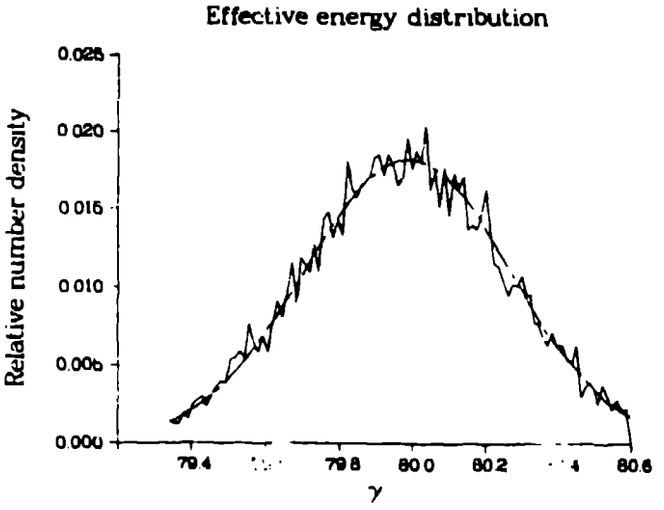

Fig. 11. Effective energy distributions in the limit $\epsilon \Rightarrow 0$. The solid line plots the distribution due to a thousand electrons randomly sampled from a gaussian distribution in energy spread while the dashed line plots the analytic effective energy distribution functio: $F(\gamma_{eff})$. The width of the distribution is given by the intrinsic energy spread, $\Delta\gamma$.

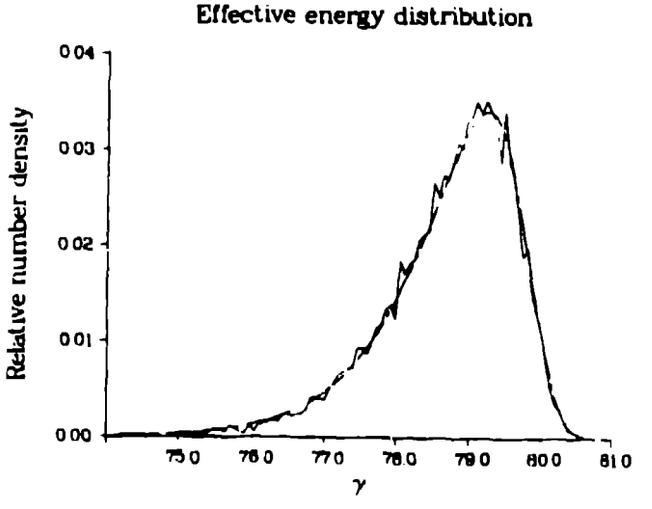

Fig. 12. Effective energy distributions for a beam with large emittance. The solid line plots the distribution due to a thousand electrons randomly sampled from gaussian distributions in emittance and energy spread while the dashed line plots the analytic effective energy distribution function $F(\gamma_{eff})$. Note the characteristic low energy tail due to the finite transverse velocity that slows the electron's axial speed.

C. Small-Signal Gain

The investigation of the small-signal gain for a FEL using an electron beam with a specified energy distribution has previously been performed.[24,25] An integral equation is obtained by combining the optical field and phase equations in the limit of weak optical fields (the small signal regime). The analysis gives the evolution of the optical field in the form

$$e_s(z) = e_{s0} + \frac{i\tilde{J}}{2}\int_0^{z/L_w} dp \int_0^p dq q \tilde{F}(q) e^{-i\nu_0 q} a_s(p-q) \tag{40}$$

where $\tilde{F}(q)$ is proportional to the Fourier transform of the effective energy distribution and $\nu_0 = 4\pi N_w(\gamma_0/\gamma_s - 1)$ is the detuning at the intrinsic mean energy, γ_0, with respect to the resonant energy, γ_s. The dimensionless optical field strength is given by

$$e_s(z) = 2N_w\pi|e|a_w[J_0(\xi) - J_1(\xi)]L_w E(z)/(\gamma^2 mc^2) \tag{41}$$

where E is the electric field amplitude, $J_n(x)$ are n^{th} order Bessel functions of the first kind, $\xi = a_w^2/(4+2a_w^2)$ and

$$\tilde{J} = \frac{4N_w[e\pi a_w(J_0(\xi) - J_1(\xi))L_w]^2 n_{eb}}{\gamma^3 mc^2} \tag{42}$$

is the dimensionless current density. The electron density is given in the limit $\beta_z \Rightarrow 1$ by

$$n_{eb} = \frac{I_p}{ecA_{eb}} \tag{43}$$

where A_{eb} is the transverse area of the electron beam. Typically I_p is derated by the factor of 0.8 to account for the degradation in gain caused by micropulse effects. The transform of the energy distribution function required to evaluate Eq. 40 is given in terms of Eq. 36 by

$$\tilde{F}(q) = e^{i\nu_0 q}\int_{-\infty}^{\infty} d\nu e^{-i\nu q}\int_0^{\infty} d\gamma_{eff}\delta[\nu - 4\pi N_w(\gamma_{eff}/\gamma_s - 1)]F(\gamma_{eff}) \tag{44}$$

for an azimuthally symmetric electron beam. Evaluating the integrals one finds[22]

$$\tilde{F}(q) = \frac{e^{-\Gamma^2\Delta\gamma^2/4}}{\left[1 - i\Gamma\left(\frac{\gamma_0^2 a_w e}{2\lambda_w(1+a_w^2/2)}\right)\right]^2} \tag{45}$$

where

$$\Gamma = \frac{4\pi N_w}{\gamma_s}q \tag{46}$$

Using Eq. 45 one can numerically evaluate the integrals in Eq. 40 to determine the small signal field amplitude inside the wiggler. A gain detuning curve can be produced by scanning the resonant signal energy, γ_s, around the mean energy, γ_0. This corresponds to scanning the optical wavelength around the desired optical wavelength, λ_s as seen from Eq. 26. Figure 13 shows an example of a typical detuning curve. Note that the gain is zero on

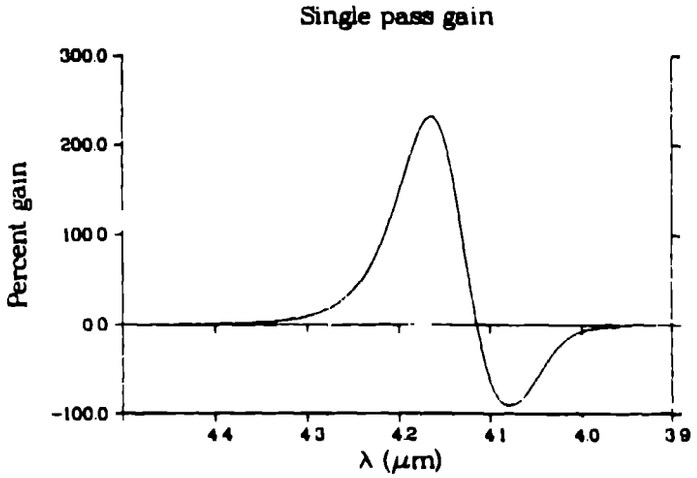

Fig. 13. Plot of small signal gain versus wavelength detuning for the effective energy distribution $F(\gamma_{eff})$. The asymmetry in the curve is due to the asymmetry in the energy distribution.

resonance. Since the peak gain is desired at the resonant wavelength, the wiggler magnetic field can be slightly adjusted to position the peak gain point at the desired wavelength. The modified magnetic vector potential is given by

$$a_w|_{new} = \sqrt{2[(1 + a_w^2/2)\frac{\lambda_{sp}}{\lambda_s} - 1]}\Bigg|_{old} \tag{47}$$

where λ_{sp} is the wavelength where the peak gain appears. The modified magnetic field can then be determined using Eq. 27. With the peak gain shifted to λ_s, the small signal electric field amplitude as a function of distance through the wiggler, is known. This formulation assumes that the FEL remains in the small signal regime and therefore does not predict where saturation occurs. The location of the saturation point requires a separate argument that will be discussed in the following section.

D. Efficiency and Gain

In the last few subsections a constant period wiggler was designed and its optimized small signal gain was determined. If the optical field amplitude in the wiggler does not saturate, the efficiency of the interaction can easily be determined. The field amplitude at the wiggler exit is given by

$$E_{exit}^2 = E_{in}^2(1 + G) \tag{48}$$

where E_{in} is the electric field at the wiggler entrance and G is the power gain from the small signal calculation. The efficiency of the untapered wiggler is given by

$$\eta_{untap} = \frac{0.7 P_{in} G}{P_{eb}} \tag{49}$$

where P_{eb} is the peak power in the electron beam and P_{in} is the power injected into the wiggler. The 0.7 coefficient represents the reduction in efficiency caused by the electrons in the wings of a gaussian axial electron beam pulse that do not interact effectively with the optical micropulse.

To increase the efficiency of a FEL design, the optical wave must saturate so that the wiggler magnetic vector potential can be tapered. Tapering allows the ponderomotive wave to remain in phase with the electron beam as it loses energy to the optical wave. Saturation will occur after the electrons execute one-half synchrotron period. The electric field at saturation, E_{sat}, can be determined by energy conservation between the electron beam and the optical wave. The energy lost by the electron beam after one-half synchrotron oscillation can be expressed

$$\delta E_{lost} \simeq n_{eb}(\gamma_0 - 1)mc^2 \frac{1}{2N'_w}\left[1 - \exp\left\{-\frac{(\gamma_p - \gamma_\phi)}{2\Delta\gamma_{eff}}\right\}\right] \tag{50}$$

where where n_{eb} is the average electron density in the electron beam, $(\gamma_0 - 1)mc^2$ is the kinetic energy per electron, $1/2N'_w$ is the maximum energy conversion efficiency in an untapered wiggler with N'_w periods[26], and

$$\left[1 - \exp\left\{-\frac{(\gamma_p - \gamma_\phi)}{2\Delta\gamma_{eff}}\right\}\right] \tag{51}$$

represents the fraction of electrons that can rotate coherently in the ponderomotive potential well (i.e. the bucket)[27,28]. The quantities γ_p and $\Delta\gamma_{eff}$ represent the peak of the effective energy distribution and the effective energy half-width, respectively. The energy of the ponderomotive wave, γ_ϕ, is obtained by solving Eq. 26 for γ. For an electron beam of cross-sectional area, $A_{eb} = \pi r^2$, and an optical mode with transverse area, $A_s = \pi w^2/2$ (where w is the optical spotsize), energy conservation dictates

$$A_s\frac{E^2_{sat}}{8\pi} = A_s\frac{E^2_{in}}{8\pi} + A_{eb}\left(\frac{0.8I_p}{ecA_{eb}}\right)\frac{1}{2N'_w}(\gamma_0 - 1)mc^2\left[1 - \exp\left\{-\frac{(\gamma_p - \gamma_\phi)}{2\Delta\gamma_{eff}}\right\}\right] \tag{52}$$

where the factor containing the peak current, I_p also includes explicitly the 0.8 derating factor. Using Eq. 48 and 52 the gain at saturation can be expressed

$$G_{sat} = \frac{A_{eb}}{A_s}\left(\frac{\omega_p}{\omega_s}\right)^2 \frac{1}{a^2_{s,in}}\frac{\gamma - 1}{N'_w}\left[1 - \exp\left\{-\frac{(\gamma_p - \gamma_\phi)}{2\Delta\gamma_{eff}}\right\}\right] \tag{53}$$

where ω_p/ω_s is the ratio of the derated plasma frequency and the optical frequency. Since the small-signal analysis gives the gain as a function of position through the wiggler, one can determine where the small-signal gain is equal to the saturated gain, G_{sat}, thereby giving the saturation position, L_{sat}. Some error will be introduced due to the fact that the actual gain begins roll over as one approaches saturation with respect to the small signal gain profile. Thus the predicted length required to reach saturation is shorter than the actual saturation length. However, this error is usually small with respect to the total wiggler length.

If the untapered wiggler length is smaller than the total length of the wiggler, the remaining length can be tapered to improve the overall FEL efficiency. The rate at which

the wiggler can be tapered is determined by the FEL configuration and the need to prevent the majority of the electrons in the ponderomotive bucket from being lost. Through analysis of optimized taper INEX designs the following rule of thumb has been adopted for the average change in a_w with respect to distance:

$$\frac{\Delta a_w}{\Delta z} = \begin{cases} 1.2 \times 10^{-3}/\lambda_w & \text{for oscillators} \\ 2.0 \times 10^{-3}/\lambda_w & \text{for amplifiers} \end{cases} \quad . \tag{54}$$

The wiggler vector potential at the end of the wiggler is

$$a_{w,end} = a_{w,in} - \frac{\Delta a_w}{\Delta z}(L_w - L_{sat}) \quad . \tag{55}$$

The efficiency of the taper section can then be approximated by

$$\eta_{tap} = 0.7\sqrt{1 - \frac{1 + a_{w,end}^2/2}{1 + a_{w,in}^2/2}}\left[\frac{1}{2} + 0.2\left(1 - e^{-\delta\gamma/\Delta\gamma_{eff}}\right)\right]\left(1 - e^{-\delta\gamma/\Delta\gamma_{eff}}\right) \quad , \tag{56}$$

where the square root term represents the efficiency of a single electron decelerated from $a_{w,in}$ to $a_{w,end}$, the factor of 1/2 represents the nominal fraction of electrons trapped in the ponderomotive bucket, the 0.2 term (including its exponential multiplying factor) gives the possible enhancement in trapping efficiency caused by prebunching, and the final term involving the exponential represents the degradation in trapping caused by emittance and intrinsic energy spread. The factor $\delta\gamma$ is the bucket height (at the entrance to the taper section) given by[28]

$$\delta\gamma = \left[\frac{a_w a_s \lambda_w [J_0(\xi) - J_1(\xi)]}{\lambda_s}\right]^{1/2} \tag{57}$$

where a_s is the optical vector potential defined in analogy with Eq. 27 as

$$a_s = \frac{|e|E(z)\lambda_s}{2\pi mc^2} \quad . \tag{58}$$

The effective energy spread of the electron beam, $\Delta\gamma_{eff}$ was previously calculated from the half-width of the effective energy distribution. Again, the 0.7 coefficient represents the reduction in efficiency due to the Gaussian micropulse shape.

The resultant efficiency from both sections of the wiggler the wiggler can now be expressed

$$\eta_{tot} = \eta_{untap} + \eta_{tap} \tag{59}$$

and including degradation of the efficiency caused by slippage gives

$$\eta = \eta_{tot}(1 - e^{-\tau_{pulse}/\tau_{slip}}) \tag{60}$$

for the overall single pass efficiency. In Eq. 60, $\tau_{slip} = N_w\lambda_s/c$ is the slippage of the electrons from the optical pulse at the end of the wiggler and τ_{pulse} is the axial electron micropulse width. The corresponding wiggler gain is

$$G = \frac{\eta P_{eb}}{P_{in}} \quad . \tag{61}$$

As previously stated, P_{in} is the optical power at the entrance to the wiggler. In the case of an amplifier, this power is provided by by an external laser and must be specified. For an oscillator, P_{in} is scanned until the gain through the wiggler is equal to the losses of the resonator. The losses include both outcoupled power and losses caused by absorption and diffraction beyond the edges of the mirrors.

E. FEL Optics

Resonator optics are required to manipulate the tightly collimated optical radiation produced in the wiggler. In the case of an amplifier, the radiation spot size must be expanded up to a size that can be handled by the beam control system. For an oscillator, optics must provide the required feedback and output coupling. A ring resonator configuration incorporating grazing incidence optics is typically considered for high power oscillator operation. The size of the mirrors and the overall resonator are determined by the average optical power extracted inside the wiggler, the absorption coefficient of the mirror material with respect to optical wavelength and the angle of incidence, the output coupling percentage of the cavity and the general resonator layout.

A schematic of a ring resonator is shown in Fig. 14. The power entering the wiggler is represented by P_{in}, while the power exiting the wiggler after amplification is denoted

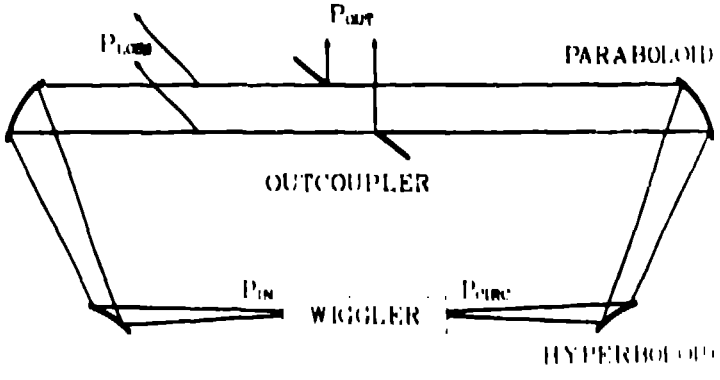

Fig. 14. Schematic representation of a FEL ring resonator. The focus is assumed to be at the center of the wiggler.

P_{circ} since this is the power that circulates in the cavity. Some type of output coupler is assumed to exist in the backleg of the resonator which extracts P_{out} watts. Other losses in the resonator including those due to absorption and diffraction beyond the mirror edges are given by P_{loss}. The gain required in the wiggler to compensate for outcoupling and losses is

$$G = \frac{P_{circ}}{P_{in}} - 1 \tag{62}$$

and with reference to Fig. 14 this becomes

$$G = \frac{P_{circ}}{P_{circ} - P_{out} - P_{loss}} - 1 \quad . \tag{63}$$

If we define the outcoupled fraction η_{out} so that $P_{out} = \eta_{out} P_{circ}$ and the resonator efficiency by

$$\eta_r = \frac{P_{out}}{P_{out} + P_{loss}} \tag{64}$$

the required wiggler gain becomes

$$G = \frac{\eta_{out}/\eta_r}{1 - \eta_{out}/\eta_r} \quad . \tag{65}$$

If the small-signal gain of the wiggler does not exceed the gain in Eq. 65, the oscillator cannot startup and only spontaneous emission will be generated.

The placement of the mirrors of the resonator is determined by the spotsize (i.e. footprint) of the light on the mirror surface, the average optical power of the light, P_{circ}, the reflectivity of the mirror material, R, and the maximum allowable intensity absorption, I_{max}. The spotsize is given in terms of the Rayleigh range, z_r and the optical wavelength by[29]

$$w^2 = \frac{z_r \lambda}{\pi}[1 + (z/z_r)^2] \quad , \tag{66}$$

where z is the distance from the focus to the position of interest. The spotsize of the intensity distribution on a planar surface whose normal is at angle θ from the axis of the optical beam is

$$A = \frac{\pi w^2}{2\cos\theta} \quad . \tag{67}$$

Knowing that the total power absorbed is given by

$$I_{max} = P_{circ}(1 - R)/A \quad , \tag{68}$$

one can make use of Eq. 66 and solve for the position z of the mirror yielding

$$z = z_r \sqrt{\frac{2P_{circ}(1 - R)\cos\theta}{z_r \lambda_s I_{max}} - 1} \tag{69}$$

for the placement of the first hyperboloid.

The radius of curvature of the optical wavefronts (near the optical axis) at this location is

$$R_c = z[1 + (z_r/z)^2] \quad . \tag{70}$$

The hyperboloid modifies the radius of curvature of the phase fronts. The curvature of the optical wave and the mirror surface are related by the mirror magnification, M through

$$R_{mir} = 2\frac{MR_c}{M - 1} \quad . \tag{71}$$

After reflection, the new curvature can be expressed

$$R_p = \frac{1}{1/R_c - 2/R_{mir}} = MR_c \quad . \tag{72}$$

The new Rayleigh range, image spotsize and image focus position are given by

$$z_r = \frac{\tilde{z}_r}{1 + (\tilde{z}_r/R_p)^2} \tag{73}$$

$$w_0 = \frac{w}{\sqrt{1 + (\tilde{z}_r/R_p)^2}} \tag{74}$$

$$z_f = \frac{-R_p}{1 + (R_p/\tilde{z}_r)^2} \tag{75}$$

where

$$\tilde{z}_r = \pi w^2/\lambda \tag{76}$$

is a fiducial range. The position of the paraboloid can now be determined by using the results of Eqs. 72 through 74 in Eq. 69. This gives the resonator half-size for oscillators or the size of the beam expansion optics for amplifier applications. The physical size of each mirror is determined by specifying the ratio of the mirror diameter to the optical spotsize. This ratio is typically 3 to 5 depending on the power inside the resonator and the desired resonator efficiency.

VI. SUMMARY

The Integrated Numerical Experiment (INEX) has proven to be a successful method for FEL design. However, for a number of reasons, the INEX approach is difficult to apply to a trade-off or initial design study. The INEX calculation is best suited for final design. The FELPPC code has been developed to overcome the disadvantages associated with the INEX approach. Relatively simple but realistic models for the accelerator, FEL interaction, and optics have been developed. With these models subsystem elements have been developed. FELPPC has eleven subsystem elements to calculate FEL performance: rf power, accelerator injector, accelerator beamline, magnetic buncher, magnetic bend, oscillator, amplifier, energy recovery decelerator, electron beam dump, beam control system, and output beam director. Each subsystem element provides the detailed information required to estimate mass, cost, and size from a parts count. With these subsystem elements a system-like model for the FEL configuration can be constructed. FELPPC can calculate a number of FEL configurations: 1) oscillator, 2) spontaneous-emission amplifier, 3) conventional-laser driven amplifier, 4) master-oscillator power-amplifier, or 5) single-accelerator master-oscillator power-amplifier. Because FELPPC can perform a FEL calculation in less than 30 seconds, trade-off and initial design studies of complex configurations can be completed in a short period of time.

Since much of the interest in FELs is directed toward applications, the physics of the particular application of interest is incorporated as a subsystem element into FELPPC. In this fashion, a relevant trade-off or initial design study is performed in the context of the application. FELPPC operates from a detailed physics description of specified hardware to obtain the FEL performance from which mass, cost, and size are determined. In general, there is no guarantee that FELPPC can provide a design with the performance required for a particular application. The application subsystem is simply used as a "metric" to judge the physics and technology implications of a particular FEL configuration.

Depending upon the FEL configuration and application, hundreds of independent variables may be required to describe the problem. As a result, some method is required to investigate the complicated nonlinear space described by FELPPC. At present, a neural net approach is being used for this purpose. To obtain optimal performance the neural net and FELPPC are combined with an optimization approach. The final design is then developed using INEX from the initial information provided by FELPPC.

ACKNOWLEDGEMENTS

The authors gratefully acknowledge B. Birkel, G. Busch, B. Carlsten, D. Cooper, R. Erickson, P. LeDelfe, J. Merson, P. Morton, and R. Tokar for their contributions to the accelerator, FEL, and space-based subsystem model development. The development of the FELPPC code was funded and supported by the U. S. Department of Defense, Army Strategic Defense Command, under the auspices of the U. S. Department of Energy.

REFERENCES

1. L. E. Thode, Ground Based FEL Program Review (August, 1987).

2. R. W. Hockney and J. W. Eastwood, Computer Simulation Using Particles (McGraw Hill, New York, 1979).

3. M. E. Jones, " Electromagnetic PIC Codes with Body-Fitted Coordinates," Proceedings of the 12th Conf. on Num. Sim. of Plasmas (San Francisco, CA, 1987).

4. L. Young and D. Chan, extended version of the standard PARMELA code including longitudinal and transverse wakefields, cavity asymmetry, three-dimensional space charge, misalignments, and jitter, private communication.

5. B. McVey, "Three-dimensional Simulations of Free Electron Laser Physics," Proc. of the 7th International Conference on Free Electron Lasers (Tahoe City, CA, 1985).

6. R. Klatt, F. Krawczyk, W. R. Novender, C. Palm, T. Weiland, B. Steffen, T. Barts, M. J. Browman, R. K. Cooper, C. T. Mottershead, G. Rodenz, and S. G. Wipf, "MAFIA - A Three-Dimensional Electromagnetic CAD System for Magnets, RF Structures, and Transient Wake-Field Calculations," Proc. 1986 Linear Accelerator Conference, Stanford Linear Accelerator Center report SLAC-303, 276 (1986).

7. T. Weiland, "Transverse Beam Cavity Interaction, Part II: Long Range Forces," Deutsches Elektronen Synchrotron report DESY 83-005 (1983).

8. T. Weiland, "Transverse Beam Cavity Interaction, Part I: Short Range Forces," Nucl. Instr. and Meth. **212**, 13 (1983).

9. K. Halbach and R. F. Holsinger, "SUPERFISH—A Computer Program for Evaluation of RF Cavities with Cylindrical Symmetry," Part. Accel. 7, 213 (1976).

10. "GLAD Command Descriptions," Applied Optics Research, Albuquerque, NM (August, 1985).

11. "OASIS Users Manual," Rocketdyne Division, Rockwell International Corporation, Albuquerque, NM (August 30, 1985). OASIS2 is similar to GLAD but can calculate polarization effects.

12. L. E. Thode, "IFEL: Integrated FEL Numerical Experiment: Injector, Accelerator, Wiggler, and Optics," Linear Accelerator Conference and Beam Optics Workshop (San Diego, CA, 1988); unpublished.

13. D. W. Feldman, H. Takeda, R. W. Warren, J. E. Sollid, W. E. Stein, W. J. Johnson, A. H. Lumpkin, and R. B. Feldman, "High Extraction Efficiency Experiments with the Los Alamos Free Electron Laser," Nucl. Instr. and Meth. **A285**, 11 (1989); B. E. Carlsten, J. C. Goldstein, and B. D. McVey, private communication.

14. R. P. Lippmann, "An Introduction to Computing with Neural Nets," IEE ASSP Magazine (April, 1987).

15. "Historian Users Guide," Opcode, Inc. (1978).

16. J. M. Hurford, "Mapper Version 4.0 Summary," Los Alamos National Laboratory Computer Graphics Documentation GR830.1 (August, 1983).

17. J. L. Merson and R. K. Cooper, "180-degree bend for SBFEL," Los Alamos National Laboratory memorandum AT-6:TM-89-47 (October 18, 1989); P. Morton, private communication.

18. K. L. Brown, "First- and Second-Order Charged Particle Optics," Stanford Linear Accelerator Center report SLAC-PUB-3381 (July, 1984).

19. K. C. D. Chan and J. S. Fraser, "Minimum Beam-Energy Spread of a High-Current RF Linac," 1987 IEEE Particle Accelerator Conference (Washington, D. C., March, 1987); IEEE catalog no. 87CH2387-9, p. 1075.

20. R. L. Gluckstern, R. K. Cooper, and P. J. Channell, "Cumulative Beam Breakup in RF Linacs," Part. Accel. **16**, 125 (1985).

21. R. L. Gluckstern and F. Neri, "Beam Breakup with Coupling Between Cavities," Part. Accel. **25**, 11 (1989).

22. C. J. Elliott, M. J. Schmitt, and B. D. McVey, to be published.

23. M. Abramowitz and I. A. Stegun, **Handbook of Mathematical Functions** (National Bureau of Standards, Washington, D. C., 1972).

24. W. B. Colson, J. C. Gallardo, and P. M. Bosco, "Free-Electron Laser Gain Degradation and Electron-Beam Quality," Phys. Rev. **A34**, 4875 (1986).

25. W. B. Colson and J. Blau, "Free-Electron Laser Theory in Weak Optical Fields," Nucl. Instr. and Meth. **A259**, 198 (1987).

26. N. M. Kroll, P. L. Morton, and M. N. Rosenbluth, "Free-Electron Lasers with Variable Parameter Wigglers," IEEE J. Quantum Electron, **QE-17**, 1436 (1981).

27. L. E. Thode, "Plasma Heating by Scattered Relativistic Electron Beam Correlations Among Experiment, Simulation, and Theory," Phys. Fluids **19**, 2684 (1976).

28. D. S. Lemons and L. E. Thode, "Linear and Nonlinear Theory of Cherenkov Maser Operation in the Intense Relativistic Beam Regime," Phys. Rev. Lett. **56**, 2684 (1986).

29. A. Yariv, **Quantum Electronics** (John Wiley and Sons, 1975)